A&A 545, A3 (2012)
DOI: 10.1051/0004-6361/201219497

Astronomy & Astrophysics

^{13}CO and C^{18}O $J = 2–1$ mapping of the environment of the Class 0 protostellar core SMM 3 in Orion B9*

O. Miettinen

Department of Physics, PO Box 64, 00014 University of Helsinki, Finland
e-mail: `oskari.miettinen@helsinki.fi`

Received 27 April 2012 / Accepted 24 July 2012

ABSTRACT

Context. Observations of molecular spectral lines provide information on the gas kinematics and chemistry of star-forming regions.

Aims. We attempt to achieve a better understanding of the gas distribution and velocity field around the deeply embedded Class 0 protostar SMM 3 in the Orion B9 star-forming region.

Methods. Using the APEX 12-m telescope, we mapped the line emission from the $J = 2–1$ rotational transition of two CO isotopologues, ^{13}CO and C^{18}O, over a 4′ × 4′ region around Orion B9/SMM 3.

Results. Both the ^{13}CO and C^{18}O lines exhibit two well-separated velocity components at about 1.3 and 8.7 km s^{-1}. The emission of both CO isotopologues is more widely distributed than the submillimetre dust continuum emission as probed by LABOCA. The LABOCA 870-μm peak position of SMM 3 is devoid of strong CO isotopologue emission, which is consistent with our earlier detection of strong CO depletion in the source. No signatures of a large-scale outflow were found towards SMM 3. The ^{13}CO and C^{18}O emission seen at ~1.3 km s^{-1} is concentrated into a single clump-like feature at the eastern part of the map. The peak H$_2$ column density towards a C^{18}O maximum of the low-velocity component is estimated to be ~10^{22} cm^{-2}. A velocity gradient was found across both the ^{13}CO and C^{18}O maps. Interestingly, SMM 3 lies on the border of this velocity gradient.

Conclusions. The ^{13}CO and C^{18}O emission at ~1.3 km s^{-1} is likely to originate from the "low-velocity part" of Orion B. Our analysis suggests that it contains high density gas (~10^{22} H$_2$ molecules per cm^2), which conforms to our earlier detection of deuterated species at similarly low radial velocities. Higher-resolution observations would be needed to clarify the outflow activity of SMM 3. The sharp velocity gradient in the region might represent a shock front resulting from the feedback from the nearby expanding H II region NGC 2024. The formation of SMM 3, and possibly of the other members of Orion B9, might have been triggered by this feedback.

Key words. stars: formation – stars: protostars – ISM: clouds – ISM: individual objects: Orion B9/SMM 3 – submillimeter: ISM – ISM: kinematics and dynamics

1. Introduction

The protostellar phase of low-mass star formation begins when a starless (prestellar) core collapses, and, after a hypothesised short-lived first-hydrostatic core stage (Larson 1969; Masunaga et al. 1998), a stellar embryo forms in its centre (the so-called second hydrostatic core; e.g., Masunaga & Inutsuka 2000). The dense cores harbouring the youngest protostars are known as the Class 0 objects (André et al. 1993, 2000). In these objects, most of the system's mass resides in the dense envelope, i.e., $M_{\rm env} \gg M_\star$, where $M_\star$ is the mass of the central protostar. For this reason, Class 0 objects, or at least the youngest of them, are expected to still represent the initial physical conditions prevailing at the time of collapse phase. Class 0 objects are characterised by accretion-powered jets and molecular outflows, which can be very powerful and highly collimated (e.g., Bontemps et al. 1996; Gueth & Guilloteau 1999; Arce & Sargent 2005, 2006; Lee et al. 2007). The statistical lifetime of the Class 0 stage is estimated to be ~1×10^5 yr (Evans et al. 2009; Enoch et al. 2009), but the exact duration of this embedded phase of evolution can be highly dependent on the initial/environmental conditions (e.g., Vorobyov 2010).

The target source of the present study is the Class 0 protostellar core SMM 3 in the Orion B9 star-forming region, which was originally discovered by Miettinen et al. (2009; Paper I) through LABOCA 870-μm dust continuum mapping of the region. SMM 3 is a strong submm emitting dust core ($S_{870} \simeq 2.5$ Jy) that is associated with a weak *Spitzer* 24-μm point source ($S_{24} \simeq 5$ mJy), and a 3.6 Jy point source at 70 μm. Using the Effelsberg 100-m telescope NH$_3$ observations, Miettinen et al. (2010; Paper II) derived the gas kinetic temperature of $T_{\rm kin} = 11.3 \pm 0.8$ K in SMM 3. Using this temperature, the core mass was determined to be $7.8 \pm 1.6\ M_\odot$, and its volume-averaged H$_2$ number density was estimated to be $1.1 \pm 0.2 \times 10^5$ cm^{-3}. In the SABOCA 350-μm mapping of Orion B9 by Miettinen et al. (2012; Paper III), SMM 3 was found to be by far the strongest source in the mapped area ($S_{350} \simeq 5.4$ Jy). We also found that it contains two subfragments, or condensations (we called SMM 3b and 3c), lying about 36″–51″ in projection from the central protostar. These correspond to 0.08–0.11 pc or ~1.7–2.3 × 10^4 AU at $d = 450$ pc[1]. Because the thermal

---

* This publication is based on data acquired with the Atacama Pathfinder EXperiment (APEX) under programme 088.F-9311A. APEX is a collaboration between the Max-Planck-Institut für Radioastronomie, the European Southern Observatory, and the Onsala Space Observatory.

[1] In this paper, we adopt a distance of 450 pc to the Orion giant molecular cloud (Genzel & Stutzki 1989). The actual distance may be somewhat smaller as, for example, Menten et al. (2007) determined a trigonometric parallax distance of 414 ± 7 pc to the Orion Nebula.

Jeans length of the core is $\lambda_J = 0.07$ pc, we suggested that the core fragmentation into condensations can be explained by thermal Jeans instability. Using the 350/870-μm flux density ratio, we determined the dust temperature of the core to be $T_{\rm dust} = 10.8^{+5.7}_{-2.6}$ K, which is very close to $T_{\rm kin}$ within the error bars. The revised spectral energy distribution (SED) of the core yielded a very low dust temperature of 8 K, and a bolometric luminosity of $L_{\rm bol} = 1.2 \pm 0.1\ L_{\odot}$. The latter is very close to the median luminosity of protostars in nearby star-forming regions, i.e., $L_{\rm med} = 1.5^{+0.7}_{-0.4}\ L_{\odot}$ (Enoch et al. 2009; Offner & McKee 2011). In Paper III, we also studied the chemistry of SMM 3. We derived a large CO depletion factor of $f_D({\rm CO}) = 10.8 \pm 2.2$, and a high level of deuterium fractionation, i.e., a N_2D^+/N_2H^+ column density ratio of 0.338 ± 0.092. In Fig. 1, we show the LABOCA 870-μm, SABOCA 350-μm, and *Spitzer* 4.5/24-μm images towards SMM 3. In Table 1, we provide an overview of the physical and chemical properties of SMM 3 derived in our previous papers.

In this paper, we discuss the results of our ^{13}CO and C^{18}O mapping observations of the environment of SMM 3. We analyse the structure of the mapped region as traced by emission from the $J = 2{-}1$ rotational transition of the above CO isotopologues. The rest of the present paper is organised as follows. Observations and data reduction are described in Sect. 2. Mapping results and analysis are presented in Sect. 3. In Sect. 4, we discuss our results, and in Sect. 5, we summarise and conclude the paper.

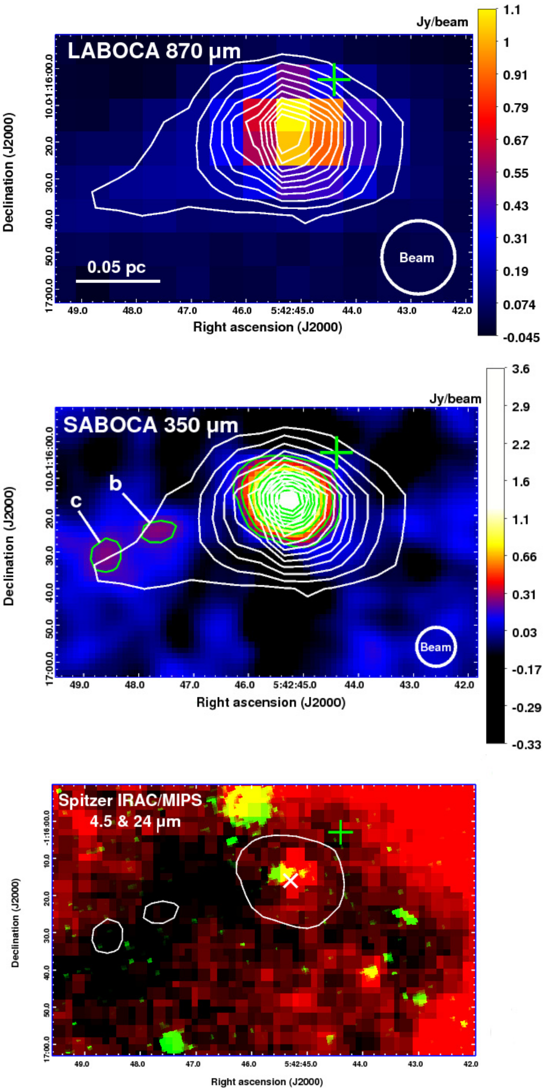

Fig. 1. LABOCA 870-μm (*top*), SABOCA 350-μm (*middle*), and a *Spitzer* IRAC/MIPS two-colour composite image (*bottom*; 4.5 μm in green and 24 μm in red) of the Class 0 protostellar core SMM 3 in Orion B9. The LABOCA and *Spitzer* images are shown with linear scaling, while the SABOCA image is shown with a square-root scaling to improve the contrast between bright and faint features. The LABOCA contours, plotted in white, go from 0.1 (∼3.3σ) to 1.0 Jy beam^{-1} in steps of 0.1 Jy beam^{-1}. The SABOCA contour levels, plotted in green, start at 3σ and are 0.18 Jy beam^{-1} × [1, 2, 4, 6, 8, 10, 12, 14, 16]. In the bottom panel, the first SABOCA contour, i.e., the 3σ emission level, is plotted in white to guide the eye, and the white cross indicates the SABOCA peak position of SMM 3. The small subcondensations SMM 3b and 3c discovered in Paper III are labelled in the middle panel. The green plus sign shows the target position of our previous molecular-line observations (i.e., the submm peak position of the LABOCA map before adjusting the pointing; see Paper III for details). A scale bar indicating the 0.05 pc projected length is shown in the bottom left of the top panel, with the assumption of a 450 pc line-of-sight distance. The effective LABOCA and SABOCA beams, ∼20″ and 10.″6, are shown in the lower right corners of the corresponding panels.

2. Observations and data reduction

The observations presented in this paper were made on 13 November 2011 using the APEX 12-m telescope located at Llano de Chajnantor in the Atacama desert of Chile. The telescope and its performance are described in the paper by Güsten et al. (2006). An area of 4′ × 4′ (0.52 pc × 0.52 pc at $d = 450$ pc) was simultaneously mapped in the $J = 2{-}1$ rotational lines of ^{13}CO and C^{18}O using the total power on-the-fly mode towards SMM 3 centred on the coordinates $\alpha_{2000.0} = 05^{\rm h}42^{\rm m}45\overset{\rm s}{.}8$, $\delta_{2000.0} = -01°16'13\overset{''}{.}0$ [(+7.″5, +3.″0) offset from the SABOCA peak position of SMM3]. At the ^{13}CO(2−1) and C^{18}O(2−1) line frequencies, 220 398.70056 and 219 560.357 MHz[2], respectively, the telescope beam size is about 28.″3 (HPBW). The target area was scanned alternately in right ascension and declination, i.e., in zigzags to ensure minimal striping artefacts in the final data cubes. Both the stepsize between the subscans and the angular separation between two successive dumps was 9.″4, i.e., about 1/3 times the beam HPBW ensuring Nyquist sampling. We note that the readout spacing 1/3 × HPBW should not be exceeded to avoid beam smearing. The integration time per dump and per pixel was 1 s.

As a frontend, we used the APEX-1 receiver of the Swedish Heterodyne Facility Instrument (SHeFI; Belitsky et al. 2007; Vassilev et al. 2008a,b). The backend was the RPG eXtended bandwidth Fast Fourier Transfrom Spectrometer (XFFTS; cf. Klein et al. 2012) with an instantaneous bandwidth of 2.5 GHz and 32 768 spectral channels. The resulting channel separation, 76.3 kHz, corresponds to about 0.1 km s^{-1} at 220 GHz.

The telescope pointing accuracy was checked by CO(2−1) cross maps of the variable star RAFGL865 (V1259 Ori), and was found to be consistent within ≲4″. The focus was checked by measurements on Jupiter. Calibration was made by means of the chopper-wheel technique and the output intensity scale given by the system is $T_A^{\star}$, which represents the antenna temperature corrected for the atmospheric attenuation. The amount of precipitable water vapour (PWV) was in the range 1.28–1.48 mm,

---

[2] The ^{13}CO(2−1) frequency was taken from Cazzoli et al. (2004), and it refers to the strongest hyperfine component $F = 5/2 - 3/2$. The C^{18}O(2−1) frequency was adopted from the JPL spectroscopic database at `http://spec.jpl.nasa.gov/` (Pickett et al. 1998).

Table 1. Summary of the properties of SMM 3.

Parameter	Value
SMM 3	
$\alpha_{2000.0}{}^{a}$	$05^{\rm h}42^{\rm m}45\overset{\rm s}{.}3$
$\delta_{2000.0}{}^{a}$	$-01°16'16''$
$\upsilon_{\rm LSR}{}^{b}$	8.68 ± 0.06 km s^{-1}
$R_{\rm eff}{}^{c}$	$13\overset{''}{.}3$ (0.03 pc)
$T_{\rm kin}{}^{d}$	11.3 ± 0.8 K
$T_{\rm dust}{}^{e}$	$10.8^{+5.7}_{-2.6}$ K
$T_{\rm dust}^{\rm SED,\,cold}$	8.0 K
$\sigma_{\rm NT}{}^{d}$	0.14 ± 0.003 km s^{-1}
$\sigma_{\rm NT}/c_{\rm s}{}^{d}$	0.7 ± 0.04
M^{f}	$7.8 \pm 1.6\ M_{\odot}/2.1 \pm 0.8\ M_{\odot}$
$\alpha_{\rm vir}{}^{g}$	0.5 ± 0.1
$N({\rm H}_2)^{f}$	$8.4 \pm 1.1 \times 10^{22}/1.0 \pm 0.3 \times 10^{23}$ cm^{-2}
$\langle n({\rm H}_2)\rangle^{f}$	$1.1 \pm 0.2 \times 10^{5}/4.0 \pm 1.5 \times 10^{5}$ cm^{-3}
$L_{\rm bol} = L_{\rm cold} + L_{\rm warm}$	$(0.3 \pm 0.1) + (0.9 \pm 0.1) = 1.2 \pm 0.1\ L_{\odot}$
$L_{\rm submm}/L_{\rm bol}{}^{h}$	0.1
$f_{\rm D}$(CO)	10.8 ± 2.2
$[{\rm N_2D^+}]/[{\rm N_2H^+}]$	0.338 ± 0.092
SMM 3b	
$\alpha_{2000.0}{}^{a}$	$05^{\rm h}42^{\rm m}47\overset{\rm s}{.}6$
$\delta_{2000.0}{}^{a}$	$-01°16'24''$
$N({\rm H}_2)^{i}$	$0.7 \pm 0.2 \times 10^{22}$ cm^{-2}
SMM 3c	
$\alpha_{2000.0}{}^{a}$	$05^{\rm h}42^{\rm m}48\overset{\rm s}{.}6$
$\delta_{2000.0}{}^{a}$	$-01°16'32''$
$N({\rm H}_2)^{i}$	$0.7 \pm 0.2 \times 10^{22}$ cm^{-2}

Notes. (a) SABOCA 350-μm peak position. (b) The LSR velocity derived from optically thin C^{17}O(2−1) line. (c) Effective radius of the "main" core as determined from the SABOCA 350-μm map. (d) Derived from NH$_3$ data. $\sigma_{\rm NT}$ and $c_{\rm s}$ are, respectively, the one dimensional non-thermal velocity dispersion and the isothermal sound speed. (e) Computed from the 350-to-870 μm flux density ratio. (f) The first value refers to the LABOCA 870-μm core, and the second one to the "main" core detected at 350 μm. (g) Virial parameter defined by $\alpha_{\rm vir} = M_{\rm vir}/M$. (h) $L_{\rm submm}$ is the submm luminosity derived by integrating the SED longward of 350 μm. (i) Calculated by making the assumption that $T_{\rm dust}$ equals the $T_{\rm kin}$ derived for the "main" core.

and the single-sideband system temperature was around 150 K (in $T_{\rm A}^{\star}$ units). The observed intensities were converted to the main-beam brightness temperature scale by $T_{\rm MB} = T_{\rm A}^{\star}/\eta_{\rm MB}$, where $\eta_{\rm MB} = 0.75$ is the main-beam efficiency at the frequencies used. The absolute calibration uncertainty is estimated to be about 10%.

The spectra were reduced and the maps were produced using the CLASS90 and GREG programmes of the GILDAS software package[3]. The individual spectra were Hanning-smoothed to improve the signal-to-noise ratio of the data. A third-order polynomial was applied to correct the baseline in the spectra. The resulting 1σ rms noise level of the average spectra are about 30 mK (in $T_{\rm MB}$) at the smoothed resolution (16 384 channels). The data were convolved with a Gaussian of 1/3 times the beam HPBW, and therefore the effective angular resolution of the final data cubes is about 30″. The average 1σ rms noise level of the completed maps ranges from 0.20 to 0.28 K per 0.2 km s^{-1} channel on a $T_{\rm MB}$ scale. The constructed data cubes were exported in FITS format for further processing in IDL.

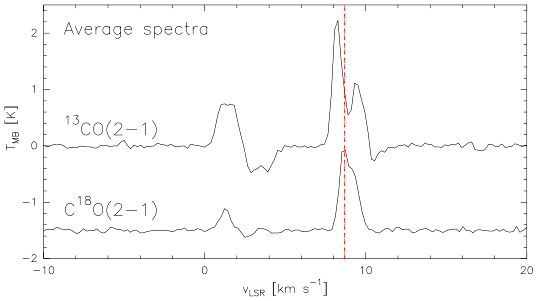

Fig. 2. Hanning-smoothed spatially averaged ^{13}CO(2−1) and C^{18}O(2−1) spectra across the mapped field. The C^{18}O(2−1) spectrum is offset by −1.45 K from zero baseline for reasons of clarity. The vertical red dashed line indicates the systemic velocity of SMM 3 derived from C^{17}O(2−1) in Paper III.

3. Mapping results and analysis

3.1. The average spectra

The average ^{13}CO(2−1) and C^{18}O(2−1) spectra are shown in Fig. 2. Both lines exhibit two well-separated velocity components: one near the systemic velocity of about 8.7 km s^{-1}, and the other at 1.3–1.4 km s^{-1}. It is not surprising that we see these lower-velocity components in the lines of CO isotopologues. The additional lines at comparable radial velocities of 1.3–1.9 km s^{-1} were already detected in the lines of N$_2$H$^+$(1−0) and N$_2$D$^+$(2−1) in Paper I, NH$_3$(1, 1) and (2, 2) in Paper II, and C^{17}O(2−1), H^{13}CO$^+$(4−3), DCO$^+$(4−3), N$_2$H$^+$(3−2), and N$_2$D$^+$(3−2) in Paper III towards other cores in Orion B9. Therefore, detection of lower-velocity line emission from CO isotopologues was expected. We note that the average ^{13}CO line near the systemic velocity of SMM 3 appears to show a blue asymmetric profile with blue peak being stronger than the red peak. The central dip also appears to be near the radial velocity derived from optically thin C^{17}O(2−1) line in Paper III. Despite of these characteristics, the double-peaked line profile is *not* caused by infall motions (e.g., Myers et al. 1996); it results from averaging over the entire mapped area, where two separate velocity components at about 8.5 and 9.5 km s^{-1} are seen. This issue will be further discussed in Sect. 3.3. The average C^{18}O line profile at the systemic velocity is nearly Gaussian, which suggests that the line is likely to be optically thin. However, a hint of the two nearby velocity components is also visible in the average C^{18}O line; the line exhibits a small "knee" at ~9.5 km s^{-1}.

It can also be seen from Fig. 2 that some of the observation OFF positions had ^{13}CO emission in the velocity regime between about 2.4 and 4.8 km s^{-1}, and between about 10.3 and 11.3 km s^{-1}, and C^{18}O emission in the range 2.0–3.3 km s^{-1}. These velocity regimes show up as artificial absorption features in the average spectra. Given the ubiquitous nature of multiple velocity components along the line of sight towards Orion B9, finding an emission free OFF position from this region can be difficult.

The main purpose of examining the average spectra is to determine the velocity range of the detected emission. This is needed to construct the line-emission maps, as will be described in the next section.

3.2. Moment maps

To display the intensity and kinematic structure of the ^{13}CO and C^{18}O line emission, we constructed the moment maps by integrating the lines over the following LSR velocity

---

[3] Grenoble Image and Line Data Analysis Software is provided and actively developed by IRAM, and is available at
`http://www.iram.fr/IRAMFR/GILDAS`

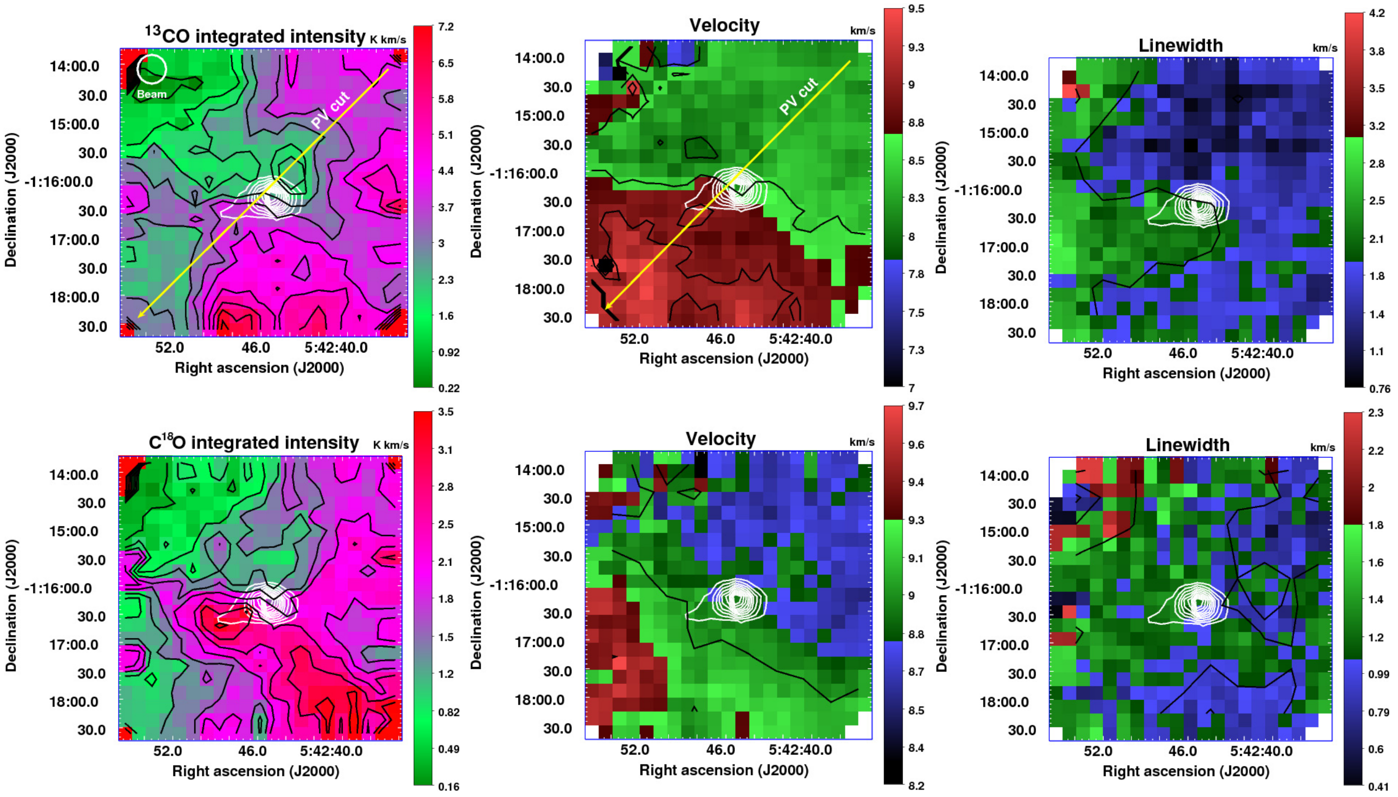

Fig. 3. The colour scale in the panels from left to right shows, respectively, the 0th (integrated intensity in $T_{\rm MB}$), 1st (intensity-weighted centroid velocity structure), and 2nd moment (intensity-weighted linewidth structure) map of the 8.7-km s^{-1} component ^{13}CO(2−1) (*top row*) and C^{18}O(2−1) emission (*bottom row*). The black contours in the upper panels, from left to right, go as follows: from 0.7 (3.2σ) to 7.0 K km s^{-1} (32σ) in steps of 0.7 K km s^{-1}; from 7 to 9.5 km s^{-1} in steps of 0.5 km s^{-1}; and from 1 to 4 km s^{-1} in steps of 1 km s^{-1}. The corresponding contours in the lower panels are from 0.4 (2σ) to 3.2 K km s^{-1} (16σ) in steps of 0.4 K km s^{-1}; from 7 to 9.5 km s^{-1} in steps of 0.5 km s^{-1}; and from 0.5 to 2 km s^{-1} in steps of 0.5 km s^{-1}. Superimposed on the maps are the LABOCA 870-μm contours in white as in Fig. 1. The yellow solid line on the top left and middle panels shows the location of the PV slice extracted for Fig. 7. The effective beam size of 30″ is shown in the upper left corner of the upper left panel.

ranges: [6.09, 10.36] km s^{-1} and [7.77, 10.36] km s^{-1} for the ^{13}CO and C^{18}O lines of the main velocity component, and [−0.07, 2.52] km s^{-1} and [0.14, 2.10] km s^{-1} for the ^{13}CO and C^{18}O lines of the lower-velocity component (at ~1.3 km s^{-1}). These line windows were selected so that the artificial absorption features discussed above are avoided. The threshold used for the moment maps was chosen to be 2 times the rms noise, i.e., 2σ.

The zeroth, first, and second moment maps (i.e., the images of integrated intensity, intensity-weighted central velocity, and intensity-weighted FWHM linewidth) of the ^{13}CO and C^{18}O emission of the main velocity component are shown in Fig. 3, while those of the lower-velocity component are shown in Fig. 4.

The map of ^{13}CO integrated intensity (upper left panel of Fig. 3) shows that there is a local emission minimum close to the SMM 3 protostellar position. This conforms to the high level of CO depletion derived from C^{17}O data. The ^{13}CO emission around SMM 3 is rather extended, which is not surprising because it arises from the lower-density gas. In contrast, the LABOCA dust continuum emission shows only the densest part of the region, i.e., SMM 3. The ^{13}CO emission appears to be strongest at about 2′ south of SMM 3, and from there it extends to the northwest part of the map. From the lower left panel of Fig. 3, it can be seen that the C^{18}O emission follows quite well the morphology of the ^{13}CO emission. There is a hint of an elongated filament-type feature along the NE to the SW direction with relatively strong emission. There appears to be a few C^{18}O maxima at the eastern part of SMM 3, one lying at the eastern tip of the 3.3σ LABOCA contour, and the other about 24″ from the central protostar.

In the case of the lower-velocity component, both the ^{13}CO and C^{18}O emission are less extended, and are instead concentrated into a single clump-like feature at the eastern part of the mapped region (left panels of Fig. 4). There is a ^{13}CO extension to the south of SMM 3 in projection, which is not seen in C^{18}O.

Interestingly, as can be seen from the first-order moment map of ^{13}CO (top middle panel of Fig. 3), there is a fairly sharp border between the two velocity fields, and SMM 3 appears to lie exactly between them, i.e., at the border of the velocity gradient. There is also a hint of increasing ^{13}CO linewidth across this border as shown in the top right panel of Fig. 3. The radial-velocity structure of C^{18}O emission is quite similar to that of ^{13}CO, but the C^{18}O linewidths show less obvious spatial trend (lower middle and right panels of Fig. 3).

Another interesting feature concerning the radial-velocity distribution is that also the lower-velocity component of C^{18}O shows a somewhat similar gradient across the map (Fig. 4; lower middle panel). Implications of the velocity gradient will be discussed further in Sect. 4.3.

3.3. Channel maps and PV plots

Velocity channel maps of the ^{13}CO and C^{18}O emission for the main velocity component are plotted in Figs. 5 and 6,

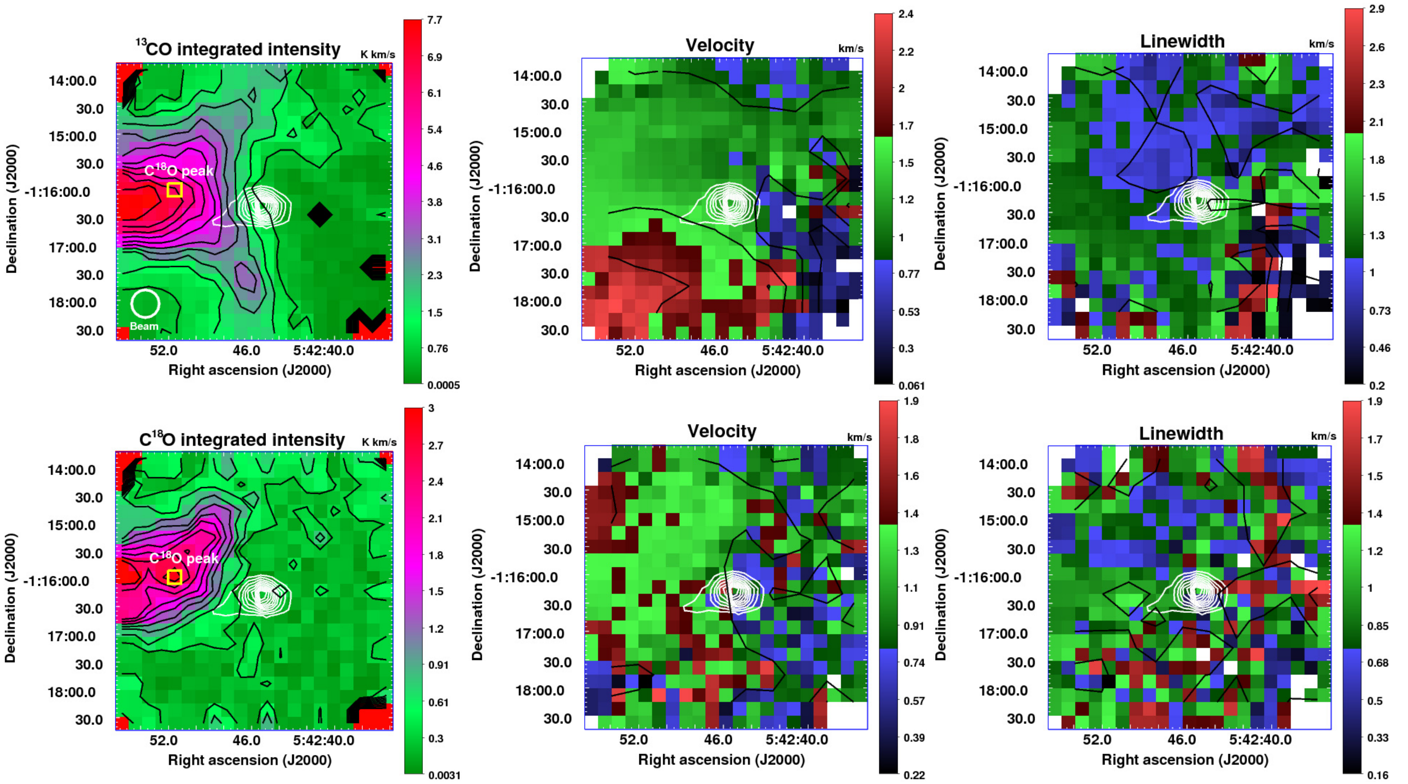

Fig. 4. Same as Fig. 3 but for the 1.3-km s^{-1} component. The black contours in the *upper panels*, *from left to right*, are plotted as follows: from 0.7 (2.7σ) to 7.0 K km s^{-1} (27σ) in steps of 0.7 K km s^{-1}; at 0.5, 1, 1.5, and 2 km s^{-1}; and from 0.5 to 2.5 km s^{-1} in steps of 0.5 km s^{-1}. In the *lower panels*, these contours are from 0.3 (1.1σ) to 2.7 K km s^{-1} (9.6σ) in steps of 0.3 K km s^{-1}; at 0.5, 1, 1.5, and 2 km s^{-1}; and at 0.5, 1, and 1.5 km s^{-1}. The C^{18}O peak position, from which the 1.3-km s^{-1} component spectra were extracted (Sect. 3.4), is indicated by a yellow box in the *left panels*. The effective beam size 30″ is shown in the lower left corner of the *upper left panel*.

respectively. As shown in these maps, extended ^{13}CO emission can be seen across the velocity range $7.86 < \upsilon_{\rm LSR} < 10.15$ km s^{-1}, while that of C^{18}O extends over a somewhat narrower range of velocities, $8.32 < \upsilon_{\rm LSR} < 9.78$ km s^{-1}.

Figure 7 shows a position-velocity (PV) diagram for ^{13}CO(2−1) emission with the direction of the cut shown in Fig. 3. The slice is taken through the entire mapped area, extending from the northwest corner to southeast corner, and its position angle, measured east of north, is PA = 135°. As shown in the top middle panel of Fig. 3, the PV slice goes across the border of the velocity gradient. The presence of two velocity components at ~8.5 and ~9.5 km s^{-1} are clearly visible in the PV plot. These velocities correspond to the NW and SE parts of the mapped area, respectively (the PV diagram of C^{18}O emission (not shown) is essentially similar).

3.4. Spectra, line parameters, and column densities at the selected positions

We extracted individual ^{13}CO and C^{18}O spectra from the map centre, i.e., near the LABOCA 870-μm peak of SMM 3. Moreover, to investigate the properties of the lower-velocity component, we extracted the ^{13}CO and C^{18}O spectra from a peak position of C^{18}O integrated intensity lying east of SMM 3 in projection (see the left panels of Fig. 4). The extracted spectra are shown in Fig. 8. The C^{18}O line towards SMM 3 shows two nearby velocity components. There is a hint of that also in the ^{13}CO spectrum. Moreover, the ^{13}CO line appears to be blueshifted with respect to the C^{18}O line, suggesting that the

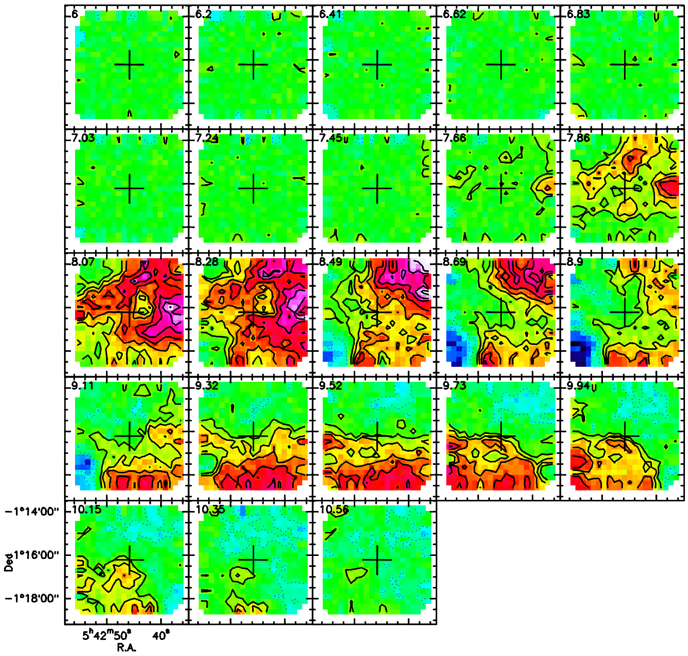

Fig. 5. Velocity channel map across 6–10.56 km s^{-1} of the ^{13}CO(2−1) line towards SMM 3. The velocity of each channel is shown in the top-left corner of each panel. The solid contours go from 0.67 to 4.67 K in steps of 0.67 K ($T_{\rm MB}$), while the dashed contours mirror negative values due to the baseline-fitting problems. The central cross on each panel indicates the map centre.

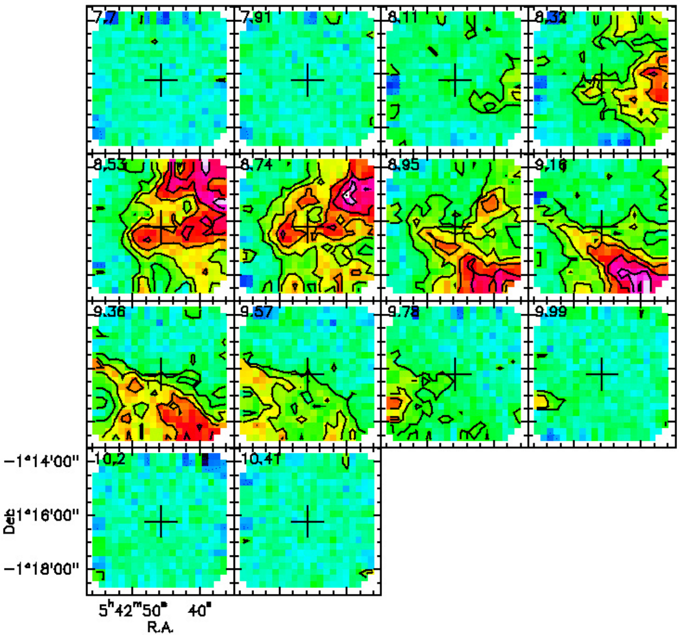

Fig. 6. Same as Fig. 5 but across 7.7–10.41 km s^{-1} of the $C^{18}O(2-1)$ line. The contours are as in Fig. 5.

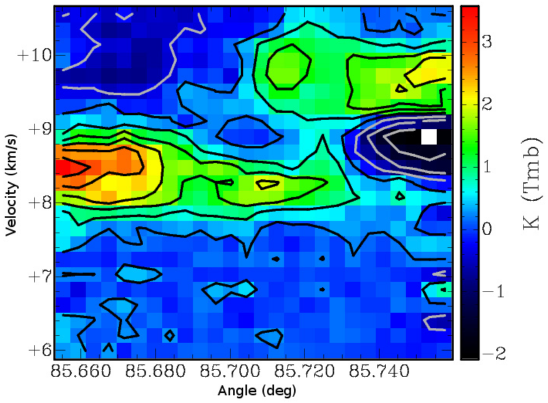

Fig. 7. Position-velocity (PV) diagram of the $^{13}CO(2-1)$ emission towards the environment of SMM 3. The PV slice runs from NW to SE, across SMM 3, as shown in Fig. 3. The black contours go from 10 to 90% of the maximum value of 3.6 K, in steps of 10%. The grey contours represent negative values.

lines originate in two different gas layers along the line of sight. In the case of the lower velocity-component spectra (lower panel of Fig. 8), the ^{13}CO line shows two velocity components around the systemic velocity of 1.38 km s^{-1} derived from $C^{18}O(2-1)$.

The line parameters of the extracted spectra are listed in Table 2. In this table, we give the offset of the target position from the map centre (in arcsec), radial LSR velocity ($\upsilon_{\rm LSR}$), FWHM linewidth ($\Delta\upsilon$), peak intensity ($T_{\rm MB}$), integrated intensity ($\int T_{\rm MB} d\upsilon$), peak line optical-thickness (τ_0), and excitation temperature ($T_{\rm ex}$). The values of $\upsilon_{\rm LSR}$ and $\Delta\upsilon$ of the $^{13}CO(2-1)$ lines were derived through fitting the hyperfine structure of the line (see Cazzoli et al. 2004), while those of $C^{18}O(2-1)$ were obtained by fitting the lines with a single Gaussian. The two nearby velocity components were fitted simultaneously but for SMM 3 we only give the parameters of the components overlaid with green lines in Fig. 8. In contrast, in the case of the $C^{18}O$ peak of the lower velocity-component, we list the ^{13}CO parameters of the component slightly redshifted from the $C^{18}O$ line velocity.

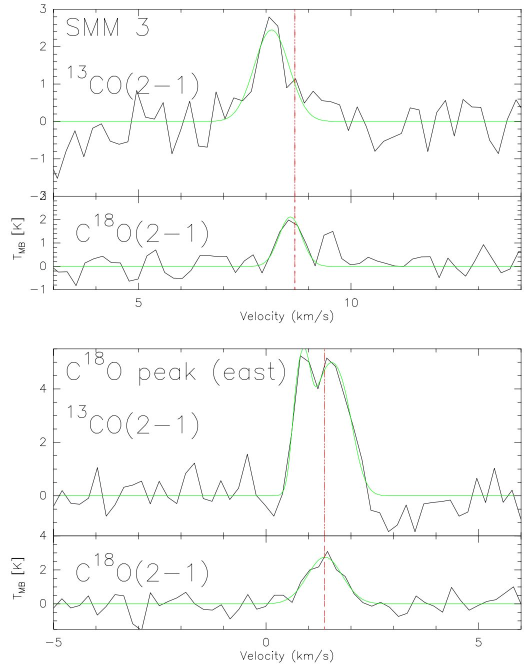

Fig. 8. The $^{13}CO(2-1)$ and $C^{18}O(2-1)$ spectra extracted towards SMM 3 (*upper panel*) and the position indicated in Fig. 4 (*lower panel*). Hyperfine-structure fits to the ^{13}CO lines, and single Gaussian fits to the $C^{18}O$ lines are overlaid in green. The red dashed line overlaid on the spectra towards SMM 3 indicates the systemic velocity of SMM 3 as derived from $C^{17}O(2-1)$ in Paper III. In *the lower panel*, the red dashed line shows the radial velocity of the $C^{18}O(2-1)$ line.

The integrated line intensities listed in Col. (7) of Table 2 were computed over the velocity range given in square brackets in the corresponding column. This way, we were able to take the non-Gaussian features of some of the lines into account. The quoted uncertainties in $\upsilon_{\rm LSR}$ and $\Delta\upsilon$ are formal 1σ fitting errors, while those in $T_{\rm MB}$ and $\int T_{\rm MB} d\upsilon$ were estimated by summing in quadrature the fitting error and the 10% calibration uncertainty.

The values of τ_0 and $T_{\rm ex}$ for the lines towards the $C^{18}O$ peak of the lower velocity-component were derived as follows. By making the assumption that the ^{13}CO and $C^{18}O$ emission arise from the same gas[4] and the two transitions have the same beam filling factor and excitation temperature[5], we can numerically estimate the line optical thicknesses from the ratio of the line peak intensities as (e.g., Myers et al. 1983; Ladd et al. 1998)

$$\frac{T_{\rm MB}(^{13}{\rm CO})}{T_{\rm MB}({\rm C}^{18}{\rm O})} \approx \frac{1-{\rm e}^{-\tau_{13}}}{1-{\rm e}^{-\tau_{18}}}. \qquad (1)$$

The peak intensities are used here rather than the integrated intensities because multiple velocity components could "contaminate" the latter values. To calculate the transition optical thicknesses, we used the CO isotopologue abundance ratio of

$$\frac{[^{13}{\rm CO}]}{[{\rm C}^{18}{\rm O}]} = \frac{[^{13}{\rm C}]}{[^{12}{\rm C}]}\frac{[^{16}{\rm O}]}{[^{18}{\rm O}]} = \frac{1}{60} \times 500 \simeq 8.3. \qquad (2)$$

---

[4] The LSR velocities of the two transitions are slightly different from each other (see Col. (4) of Table 2), so they may not be tracing exactly the same gas layers.

[5] We note that the observed ^{13}CO and $C^{18}O$ transitions have similar frequencies. Therefore, the frequency-dependent main-beam efficiency ($\eta_{\rm MB}$), and the telescope beam HPBW are also almost identical for the two transitions.

Table 2. Parameters of the spectra extracted from the selected positions.

Position	Offset^a ($''$, $''$)	Transition	$v_{\rm LSR}$ [km s^{-1}]	Δv [km s^{-1}]	$T_{\rm MB}$ [K]	$\int T_{\rm MB} {\rm d}v^b$ [K km s^{-1}]	τ_0	$T_{\rm ex}$ [K]	N [10^{15} cm^{-2}]
Main velocity component									
SMM 3	(0 , 0)	^{13}CO(2−1)	8.11 ± 0.09	0.95 ± 0.36	2.73 ± 0.45	2.61 ± 0.67 [7.17, 9.21]	–	–	–
		C^{18}O(2−1)	8.57 ± 0.05	0.63 ± 0.11	2.12 ± 0.25	1.39 ± 0.25 [8.00, 9.14]	0.2 ± 0.1^c	11.0 ± 1.0^c	0.85 ± 0.2^d
Lower-velocity component									
C^{18}O peak	(+85.5 , +14.0)	^{13}CO(2−1)	1.52 ± 0.06	0.81 ± 0.12	5.17 ± 0.61	7.05 ± 0.86 [0.21, 2.38]	$6.3^{+2.4e}_{-1.9}$	–	18.2 ± 6.8
		C^{18}O(2−1)	1.38 ± 0.06	0.97 ± 0.15	2.75 ± 0.61	2.89 ± 0.47 [0.07, 2.52]	$0.8^{+0.3e}_{-0.2}$	9.5 ± 1.8^f	2.8 ± 1.0

Notes. $^{(a)}$ Offset from the map centre in arcsec. $^{(b)}$ Integrated intensity is derived by integrating over the velocity range indicated in square brackets. $^{(c)}$ This optical thickness is estimated from that derived for C^{17}O(2−1) in Paper III, and the reported $T_{\rm ex}$ value is that of C^{17}O(2−1). $^{(d)}$ Derived from the integrated intensity under the assumption of optically thin emission. $^{(e)}$ Derived from the line intensity ratio, as described in Sect. 3.4. $^{(f)}$ Derived using the $T_{\rm MB}$ and τ_0 values of the C^{18}O line.

The adopted carbon- and oxygen-isotopic ratios are the same as those used in Paper III for a proper comparison to that work (see references therein)[6]. Consequently, the optical thickness ratio τ_{13}/τ_{18} was assumed to be equal to 8.3.

Once the optical thickness is determined, $T_{\rm ex}$ can be calculated using the radiative transfer equation (see, e.g., Eq. (1) in Paper I). In this calculation, we assumed a beam filling factor of unity, and that the background temperature is equal to the cosmic background radiation temperature of 2.725 K.

The derived values of τ_{13}, τ_{18}, and $T_{\rm ex}$ are listed on Cols. (8) and (9) of Table 2. In this table, we use the symbol τ_0 for the optical thickness to denote its peak value. The quoted uncertainties were derived from the uncertainties of the peak intensities. The ^{13}CO line appears to be optically thick, while the C^{18}O line shows a moderate optical thickness of $\tau_{18} \simeq 0.8^{+0.3}_{-0.2}$.

The total beam-averaged ^{13}CO and C^{18}O column densities were computed following Eq. (4) of Paper I. The spectroscopic parameters needed in the analysis, such as the electric dipole moments and rotational constants, were adopted from the JPL database. The derived column densities are listed in the last column of Table 2. The quoted uncertainties were propagated from those associated with $T_{\rm ex}$, Δv, and τ_0 (the average value of the $^+_-$−errors of $T_{\rm ex}$ and τ_0 were used).

3.5. CO depletion in SMM 3

In Paper III, we derived a CO depletion factor of $f_{\rm D} = 10.8 \pm 2.2$ towards SMM 3 through C^{17}O(2−1) observations (27$''\!$.8 resolution). Another estimate of $f_{\rm D}$ in SMM 3 can be obtained from the current C^{18}O data. We prefer to use C^{18}O for this analysis rather than ^{13}CO, because C^{18}O emission is more optically thin than the ^{13}CO emission. Therefore, C^{18}O is expected to trace gas deeper into the core's envelope, and being less affected by foreground emission.

The values of τ_0 and $T_{\rm ex}$ for the C^{17}O(2−1) line were derived to be 0.05 ± 0.03 and 11.0 ± 1.0 K, respectively (Paper III). As the oxygen-isotopic ratio [^{18}O]/[^{17}O] is only 3.52 (Frerking et al. 1982), it can be assumed that the C^{18}O(2−1) line is also optically thin. Under the assumption of optically thin emission ($\tau \ll 1$), and adopting $T_{\rm ex} = 11 \pm 1$ K, the C^{18}O column density computed from the integrated intensity is $N({\rm C^{18}O}) = 8.5 \pm 1.7 \times 10^{14}$ cm^{-2}.

By smoothing the LABOCA map to match the resolution of the C^{18}O map (30$''$), and regridding it onto the same pixel scale, the 870-μm peak flux density towards the (0$''$, 0$''$) position of the C^{18}O map is determined to be 0.85 Jy beam^{-1}. Using the assumption that $T_{\rm dust} = T_{\rm kin}$, and that the dust opacity per unit dust mass at 870 μm is $\kappa_{870} = 1.7$ cm^2 g^{-1} (Ossenkopf & Henning 1994; Paper I), we estimate that the corresponding H$_2$ column density is $N({\rm H_2}) = 2.5 \pm 0.3 \times 10^{22}$ cm^{-2} (see Papers I and III for further details). Therefore, the fractional abundance of C^{18}O towards the (0$''$, 0$''$) position is estimated to be $x({\rm C^{18}O}) = N({\rm C^{18}O})/N({\rm H_2}) = 3.4 \pm 0.8 \times 10^{-8}$.

To compute $f_{\rm D}$ from C^{18}O data, we need an estimate of the "canonical", or undepleted, abundance of C^{18}O. Using the standard value 9.5×10^{-5} for the abundance of the main CO isotopologue in the solar neighbourhood (Frerking et al. 1982), we can write

$$x({\rm C^{18}O})_{\rm can} = x({\rm CO})_{\rm can} \times \frac{[^{18}{\rm O}]}{[^{16}{\rm O}]} = 9.5 \times 10^{-5} \times \frac{1}{500} = 1.9 \times 10^{-7}\,. \tag{3}$$

The value of $f_{\rm D}$ is then determined to be $f_{\rm D} = x({\rm C^{18}O})_{\rm can}/x({\rm C^{18}O})_{\rm obs} = 5.6 \pm 1.3$. This is comparable within a factor of two to the value derived from C^{17}O(2−1) data. The agreement is quite good given all the assumptions used in the analysis. We note that the (0$''$, 0$''$) position of the C^{18}O map is not exactly coincident with our previous C^{17}O observation target position but the two are within the beam size of both the observations.

Following the analysis presented in Miettinen (2012, Sect. 5.5 therein), the CO depletion timescale in SMM 3 is estimated to be only $\tau_{\rm dep} \sim 1{-}3.7 \times 10^4$ yr (using the values $T_{\rm kin} = 11.3$ K and $n({\rm H_2}) = 1.1{-}4.0 \times 10^5$ cm^{-3}; see Table 1). This provides a lower limit to the age of the core.

4. Discussion

4.1. On the non-detection of molecular outflows

Because SMM 3 is an early Class 0 source, it is expected to drive a bipolar molecular outflow. The outflows can manifest themselves in broad non-Gaussian spectral-line wings. One of our original attempts of the present study was to search for outflows driven by SMM 3 through ^{13}CO observations. However, in our data, there is no evidence for a large-scale ^{13}CO outflow. In the *Spitzer*/IRAC 4.5-μm image of SMM 3 (Fig. 1; bottom panel), there are some 4.5-μm emission features that could be signatures of shock-excited material around SMM 3 (e.g., Smith

---

[6] We note that larger ratios of [^{12}C]/[^{13}C] = 77 and [^{16}O]/[^{18}O] = 560 (Wilson & Rood 1994) are often used in a similar analysis (e.g., Teyssier et al. 2002). These values lead to the ratio [^{13}CO]/[C^{18}O] ≃ 7.3.

& Rosen 2005; De Buizer & Vacca 2010). For comparison, the Class 0/I protostar IRAS 05399-0121 in Orion B9, which drives the HH 92 jet (Bally et al. 2002), exhibits spectacular IRAC 4.5-μm features along its parsec-scale bipolar jet. Clearly, higher resolution observations, and better outflow tracers, such as ^{12}CO and SiO, would be needed to clarify the outflow activity of SMM 3.

4.2. Low-velocity gas emission

As was discussed in Paper II (Sect. 5.7 therein), the lower-velocity line emission seen towards Orion B9 is likely to come from the "low-velocity part" of Orion B, which probably originates from the feedback from the massive stars of the nearby Ori OB 1b association. This fraction of the gas is likely to be located a few tens of parsecs closer to the Sun than the "regular" 9-km s^{-1} gas component (Wilson et al. 2005).

The C^{18}O column density towards the selected C^{18}O peak is $2.8 \pm 1.0 \times 10^{15}$ cm^{-2}. We can convert this to an estimate of the H$_2$ column density as

$$N(\mathrm{H_2}) = \frac{[\mathrm{H_2}]}{[^{12}\mathrm{CO}]} \times \frac{[^{12}\mathrm{CO}]}{[\mathrm{C^{18}O}]} \times N(\mathrm{C^{18}O})\,. \tag{4}$$

Using again the values $[^{12}\mathrm{CO}]/[\mathrm{C^{18}O}] = [^{16}\mathrm{O}]/[^{18}\mathrm{O}] = 500$ and $[^{12}\mathrm{CO}]/[\mathrm{H_2}] = 9.5 \times 10^{-5}$, we obtain $N(\mathrm{H_2}) = 1.5 \pm 0.5 \times 10^{22}$ cm^{-2}. This shows that the "low-velocity part" of Orion B also consists of dense gas, which conforms to our previous detection of, e.g., deuterated molecular species at comparable LSR velocities. We also note that the prestellar core SMM 7 and Class 0 protostar IRAS 05413-0104 seen towards Orion B9 have such low systemic velocities (~3.7 and ~1.5 km s^{-1}, respectively) that they are likely to be members of the low-velocity Orion B. Despite the estimated high column density of the clump-like ^{13}CO/C^{18}O feature seen in the left panels of Fig. 4, it was not seen in LABOCA 870-μm emission at the $\sim 3\sigma$ level (reflecting the strong CO depletion in the main velocity component).

4.3. On the origin of the velocity gradient and implications for the core/star formation in Orion B9

In Paper II, we speculated that the Orion B9 region has probably been influenced by the feedback from the nearby Orion OB association, or more precisely, from the Ori OB 1b subgroup. As mentioned above, this feedback is believed to be responsible for the "low-velocity part" of Orion B (Wilson et al. 2005). We believe that the discovery of a velocity gradient in the present study supports the possibility that Orion B9 region is affected by stellar feedback.

To better illustrate the larger-scale view of the surroundings of Orion B9, in Fig. 9 we show a wide-field *Herschel*/SPIRE 250-μm image[7]. A visual inspection of the image suggests that the Orion B9 region might be situated in quite a dynamic environment. Towards the south, there is the active massive star-forming region NGC 2024 some 40′ (~5.2 pc at 450 pc) from Orion B9. The northwest-southeast orientated 250-μm filament emanating from NGC 2024 is likely related to the dense molecular ridge of NGC 2024 running in the same direction (e.g., Thronson et al. 1984; Visser et al. 1998; Watanabe & Mitchell 2008). The expanding H II region of NGC 2024 appears to be interacting with the molecular ridge (Gaume et al. 1992). The majority of the members of Ori OB 1b association lie towards the west/northwest from Orion B9 (see, e.g., Fig. 1 in Wilson et al. 2005).

It is apparent from the bottom panel of Fig. 9 that the Orion B9 cores, with the possible exception of SMM 7, belong to a common northeast-southwest orientated filamentary structure. As indicated in the figure, the cores at the northeastern part of the region have a lower LSR velocity or show multiple velocity components as found in our previous papers. As discussed earlier, a gradient of increasing radial velocity from NW to SE is seen across the mapped area, and SMM 3 appears to lie on the border of the velocity jump (cf. the case of the Class 0 protostar HH211 in Perseus/IC348, Tobin et al. 2011). Interestingly, this velocity gradient appears to be orthogonal to the direction of the 250-μm filament orientated NE-SW (SMM 3 also lies on the border of the dust filament). This raises the question whether this border could be tracing a shock layer of the interacting/colliding flows, within which there is a jump in the velocity of the gas. Such interaction might have been responsible for triggering the formation of SMM 3, and (some) of the other cores in the region. It seems more likely that, instead of the influence of Ori OB 1b, the feedback from the nearby expanding NGC 2024 H II region could have compressed the inital cloud region (Fukuda & Hanawa 2000). Later, the cloud under a high pressure gradient may have fragmented into dense cores, out of which some, such as SMM 3, were collapsed into protostars sequentially.

SMM 3 showed the highest level of CO depletion among the cores studied in Paper III. This conforms to the fact that it also appears to be the densest core in Orion B9. For the core collapse induced by compression, the simulations by Hennebelle et al. (2003) suggest that the combined duration of the prestellar+Class 0 phase is $\sim 3.2 \times 10^5 - 1.3 \times 10^6$ yr (depending on the rate of compression). As mentioned earlier, the estimated CO depletion timescale in SMM 3 is $\sim 1 - 3.7 \times 10^4$ yr, which is shorter than the core evolution timescales quoted above. On the other hand, the fragmentation timescale of the core is expected to be comparable to the signal crossing time, which for SMM 3 is estimated to be $\tau_{\mathrm{cross}} = D/\sigma_{\mathrm{3D}} \sim 6.6 \times 10^5$ yr (the projected core diameter across the 3.3σ contour is 86″ or $D = 0.19$ pc, and $\sigma_{\mathrm{3D}} = \sqrt{3}\sigma_{\mathrm{1D}}$ is the three-dimensional velocity dispersion). This agrees well with the above theoretical core lifetimes. From these considerations, we suggest that the formation of SMM 3, and of some other cores in Orion B9, was triggered by feedback from NGC 2024 (dynamical compression) some several times $\sim 10^5$ yr ago (cf. Fukuda & Hanawa 2000).

To better understand the velocity structure of the region on larger scales, larger maps of molecular-line emission would be needed. We note that the star formation in Orion B9, if triggered by stellar feedback, might resemble the situations in the ρ Ophiuchus (e.g., Nutter et al. 2006) and the B59/Pipe Nebula (Peretto et al. 2012), where the star formation appears to be induced by the feedback from the Scorpius OB association.

5. Summary and conclusions

A 4′×4′ region around the Class 0 protostar SMM 3 in Orion B9 was mapped in ^{13}CO and C^{18}O $J = 2-1$ lines with the APEX

---

[7] *Herschel* is an ESA space observatory with science instruments provided by European-led Principal Investigator consortia and with important participation from NASA (Pilbratt et al. 2010). Orion B was observed as part of the "*Herschel* Gould Belt Survey (GBS)" (André et al. 2010), using the PACS (Poglitsch et al. 2010) and the SPIRE (Griffin et al. 2010) instruments. For more details, see `http://gouldbelt-herschel.cea.fr`. The data are available from the *Herschel* Science Archive (HSA) at `http://herschel.esac.esa.int/Science_Archive.shtml`

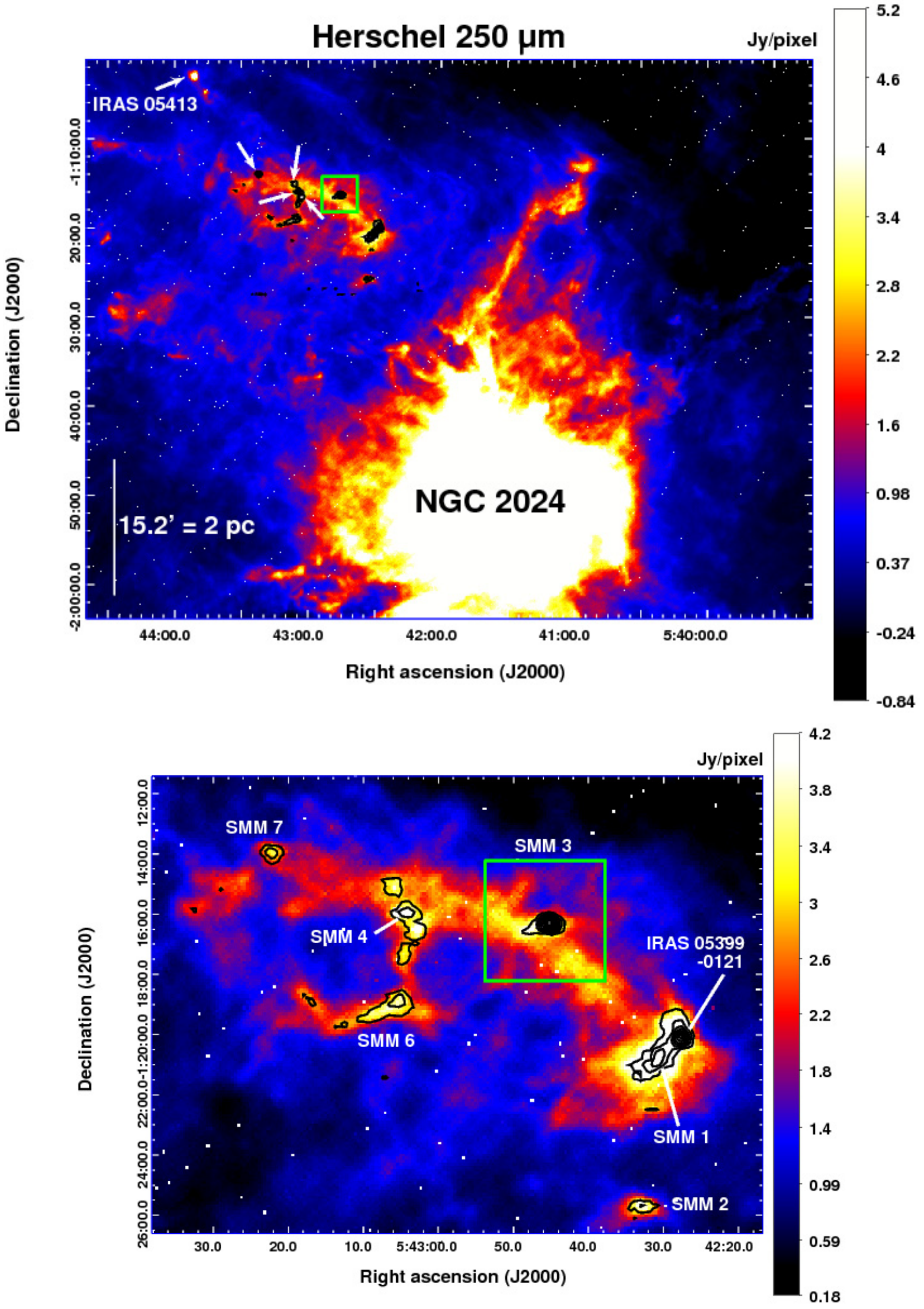

Fig. 9. *Top:* a wide-field *Herschel*/SPIRE 250-μm far-infrared image towards the Orion B9 and NGC 2024 (Flame Nebula) star-forming regions. The image is overlaid with black contours of LABOCA 870-μm dust continuum emission. The contours go from 0.1 ($\sim 3.3\sigma$) to 1.0 Jy beam^{-1} in steps of 0.1 Jy beam^{-1}. The green rectangle outlines the $4' \times 4'$ area mapped in ^{13}CO(2−1) and C^{18}O(2−1) in the present study. The white arrows indicate the cores which have a lower LSR velocity than the "main 9-km s^{-1} part" of Orion B9 or show multiple velocity components. The Class 0 protostar IRAS 05413-0104 in the northeast corner was at the border of our LABOCA map and only weakly detected (see Fig. 1 in Paper I). Note how the Orion B9 cores are associated with a NE-SW orientated filamentary structure, and the cores with lower radial velocity (or with multiple velocity components) lie at the NE part of the structure. A scale bar indicating the 2 pc projected length is shown in the bottom left, with the assumption of a 450 pc line-of-sight distance. *Bottom:* a zoomed-in view of the upper image towards Orion B9. Selected cores are labelled. The LABOCA contours are as in the upper panel.

12-m telescope. Our main results and conclusions can be summarised as follows:

1. Both lines exhibit two well separated velocity components: one at $\sim$1.3 km s^{-1} and the other at $\sim$8.7 km s^{-1}. The latter is near the systemic velocity of SMM 3. The low-velocity component was already recognised in our previous studies, and it is believed to be related to the low-velocity part of Orion B.
2. The ^{13}CO and C^{18}O emission are relatively widely distributed compared to the dust continuum emission traced by LABOCA. The LABOCA 870-μm peak position of SMM 3 is not coincident with any strong ^{13}CO or C^{18}O emission, which is in accordance with the high CO depletion factor

derived earlier by us from C^{17}O(2–1) ($f_D \simeq 10.8$). The CO depletion factor derived from C^{18}O data is within a factor of two from the previous estimate, i.e., $f_D \simeq 5.6$. No evidence for a large-scale outflow activity, i.e., high velocity line wings, was found towards SMM 3.

3. The lower-velocity (~1.3 km s^{-1}) ^{13}CO and C^{18}O emission are concentrated into a clump-like feature at the eastern part of the map. We estimate that the H$_2$ column density towards its C^{18}O maximum is ~10^{22} cm^{-2}. Therefore, the lower-velocity gas seen along the line of sight is of high density, which is consistent with our earlier detection of, e.g., deuterated molecular species (DCO$^+$, N$_2$D$^+$).
4. We observe a velocity gradient across the ^{13}CO and C^{18}O maps along the NW-SE direction (some hint of that is also visible in the lower-velocity line maps). Interestingly, SMM 3 is projected almost exactly on the border of the velocity jump. The sharp velocity-gradient border provides a strong indication that it represents an interaction zone of flow motions.
5. We suggest a possible scenario in which the formation of SMM 3, and likely some of the other dense cores in Orion B9, was triggered by an expanding H II region of NGC 2024. This collect- and collapse-type process might have been taken place some several times 10^5 yr ago. The NGC 2024 region is known to be a potential site of induced, sequential star formation (e.g., Fukuda & Hanawa 2000, and references therein). The case of Orion B9 suggests that we may be witnessing the most recent event of self-propagating star formation around NGC 2024. Larger-scale molecular-line maps would be needed for a better understanding of the larger-scale velocity structure of the region.

Acknowledgements. I thank the anonymous referee very much for his careful reading and constructive comments and suggestions which helped to improve this paper considerably. I am grateful to the staff at the APEX telescope for performing the service-mode observations presented in this paper. The Academy of Finland is acknowledged for the financial support through grant 132291. SPIRE has been developed by a consortium of institutes led by Cardiff Univ. (UK) and including: Univ. Lethbridge (Canada); NAOC (China); CEA, LAM (France); IFSI, Univ. Padua (Italy); IAC (Spain); Stockholm Observatory (Sweden); Imperial College London, RAL, UCLMSSL, UKATC, Univ. Sussex (UK); and Caltech, JPL, NHSC, Univ. Colorado (USA). This development has been supported by national funding agencies: CSA (Canada); NAOC (China); CEA, CNES, CNRS (France); ASI (Italy); MCINN (Spain); SNSB (Sweden); STFC, UKSA (UK); and NASA (USA). This research has made use of NASA's Astrophysics Data System and the NASA/IPAC Infrared Science Archive, which is operated by the JPL, California Institute of Technology, under contract with the NASA. This research has also made use of the SIMBAD database, operated at CDS, Strasbourg, France.

References

André, P., Ward-Thompson, D., & Barsony, M. 1993, ApJ, 406, 122
André, P., Ward-Thompson, D., & Barsony, M. 2000, in Protostars and Planets IV, eds. Mannings, V., Boss, A. P., & Russell, S. S. (Tucson: Univ. of Arizona Press), 59
André, P., Men'shchikov, A., Bontemps, S., et al. 2010, A&A, 518, L102
Arce, H. G., & Sargent, A. I. 2005, ApJ, 624, 232
Arce, H. G., & Sargent, A. I. 2006, ApJ, 646, 1070
Bally, J., Reipurth, B., & Aspin, C. 2002, ApJ, 574, L79
Belitsky, V., Lapkin, I., Vassilev, V., et al. 2007, in Proc. joint 32nd International Conference on Infrared Millimeter Waves and 15th International Conference on Terahertz Electronics, September 3–7 (Cardiff, Wales, UK: City Hall), 326
Bontemps, S., André, P., Terebey, S., & Cabrit, S. 1996, A&A, 311, 858
Cazzoli, G., Puzzarini, C., & Lapinov, A. V. 2004, ApJ, 611, 615
De Buizer, J. M., & Vacca, W. D. 2010, AJ, 140, 196
Enoch, M. L., Evans, N. J., II, Sargent, A. I., & Glenn, J. 2009, ApJ, 692, 973
Evans, N. J., II, Dunham, M. M., Jørgensen, J. K., et al. 2009, ApJS, 181, 321
Frerking, M. A., Langer, W. D., & Wilson, R. W. 1982, ApJ, 262, 590
Fukuda, N., & Hanawa, T. 2000, ApJ, 533, 911
Gaume, R. A., Johnston, K. J., & Wilson, T. L. 1992, ApJ, 388, 489
Genzel, R., & Stutzki, J. 1989, ARA&A, 27, 41
Griffin, M. J., Abergel, A., Abreu, A., et al. 2010, A&A, 518, L3
Gueth, F., & Guilloteau, S. 1999, A&A, 343, 571
Güsten, R., Nyman, L. Å., Schilke, P., et al. 2006, A&A, 454, L13
Hennebelle, P., Whitworth, A. P., Gladwin, P. P., & André, P. 2003, MNRAS, 340, 870
Kitsionas, S., & Whitworth, A. P. 2007, MNRAS, 378, 507
Klein, B., Hochgürtel, S., Krämer, I., et al. 2012, A&A, 542, L3
Ladd, E. F., Fuller, G. A., & Deane, J. R. 1998, ApJ, 495, 871
Larson, R. B. 1969, MNRAS, 145, 271
Lee, C.-F., Ho, P. T. P., Hirano, N., et al. 2007, ApJ, 659, 499
Masunaga, H., & Inutsuka, S.-I. 2000, ApJ, 531, 350
Masunaga, H., Miyama, S. M., & Inutsuka, S.-I. 1998, ApJ, 495, 346
Menten, K. M., Reid, M. J., Forbrich, J., & Brunthaler, A. 2007, A&A, 474, 515
Miettinen, O. 2012, A&A, 542, A101
Miettinen, O., Harju, J., Haikala, L. K., Kainulainen, J., & Johansson, L. E. B. 2009, A&A, 500, 845 (Paper I)
Miettinen, O., Harju, J., Haikala, L. K., & Juvela, M. 2010, A&A, 524, A91 (Paper II)
Miettinen, O., Harju, J., Haikala, L. K., & Juvela, M. 2012, A&A, 538, A137 (Paper III)
Motoyama, K., & Yoshida, T. 2003, MNRAS, 344, 461
Myers, P. C., Linke, R. A., & Benson, P. J. 1983, ApJ, 264, 517
Myers, P. C., Mardones, D., Tafalla, M., et al. 1996, ApJ, 465, L133
Nutter, D., Ward-Thompson, D., & André, P. 2006, MNRAS, 368, 1833
Offner, S. S. R., & McKee, C. F. 2011, ApJ, 736, 53
Ossenkopf, V., & Henning, T. 1994, A&A, 291, 943
Peretto, N., André, P., Könyves, V., et al. 2012, A&A, 541, A63
Pickett, H. M., Poynter, I. R. L., Cohen, E. A., et al. 1998, J. Quant. Spec. Radiat. Transf., 60, 883
Pilbratt, G. L., Riedinger, J. R., Passvogel, T., et al. 2010, A&A, 518, L1
Poglitsch, A., Waelkens, C., Geis, N., et al. 2010, A&A, 518, L2
Schöier, F. L., van der Tak, F. F. S., van Dishoeck, E. F., & Black, J. H. 2005, A&A, 432, 369
Smith, M. D., & Rosen, A. 2005, MNRAS, 357, 1370
Teyssier, D., Hennebelle, P., & Pérault, M. 2002, A&A, 382, 624
Thronson, H. A., Jr., Lada, C. J., Schwartz, P. R., et al. 1984, ApJ, 280, 154
Tobin, J. J., Hartmann, L., Chiang, H.-F., et al. 2011, ApJ, 740, 45
Vassilev, V., Meledin, D., Lapkin, I., et al. 2008a, A&A, 490, 1157
Vassilev, V., Henke, D., Lapkin, I., et al. 2008b, IEEE Microwave and Wireless Components Letters, 18, 55
Visser, A. E., Richer, J. S., Chandler, C. J., & Padman, R. 1998, MNRAS, 301, 585
Vorobyov, E. I. 2010, ApJ, 713, 1059
Watanabe, T., & Mitchell, G. F. 2008, AJ, 136, 1947
Wilson, T. L., & Rood, R. 1994, ARA&A, 32, 191
Wilson, B. A., Dame, T. M., Masheder, M. R. W., & Thaddeus, P. 2005, A&A, 430, 523